Multifrequency transcranial ultrasound holography with acoustic lenses

M. Daniel,[1,*] D. Attali,[1,2] T. Tiennot,[1] M. Tanter,[1] and JF. Aubry[1,†]

[1] *Physics for Medicine Paris, Inserm U1273, ESPCI Paris, PSL University, CNRS UMR 8063, 75015 Paris, France*
[2] *GHU-Paris Psychiatrie et Neurosciences, Hôpital Sainte Anne, Université Paris Cité, 75014 Paris, France*

(Received 27 September 2023; revised 27 November 2023; accepted 5 December 2023; published 9 January 2024)

Focusing ultrasound through the skull requires the accurate correction of skull-induced aberrations. Acoustic lenses provide an inexpensive and effective measure for correcting these distortions. This study explores a phase unwrapping technique for designing multifrequency acoustic lenses coupled with geometrically focused transducers. Here, we demonstrate numerically and theoretically that, in a homogeneous medium and for a single target steered from the natural focus of the transducer, a wrapped lens can only work at its design frequency, while a phase unwrapped lens is broadband. This concept is further explored in experiments where three human skulls are inserted between a transducer and its natural focus. Unwrapped lenses are used to correct for the skull aberrations at multiple frequencies and are compared with their wrapped counterparts. Such experiments demonstrate that only the unwrapped lenses are capable of correcting for skull aberrations in a broad range of frequencies. At the design frequency of the lenses, the unwrapped lenses perform quantitatively better than their wrapped counterparts since the average intensity behind the three skulls is found to be 49% lower with a phase wrapped lens compared with a phase unwrapped lens, even if both allow the qualitative refocusing of the wave at the desired targets. In addition, such results confirm the necessity of correcting for skull aberrations, since the field may be highly distorted in the absence of aberration correction.

DOI: 10.1103/PhysRevApplied.21.014011

I. INTRODUCTION

Focused ultrasound is an emerging and promising technology that has been successfully used to treat patients with a variety of indications [1–3]. Targeting the brain with ultrasound has long been hampered by the defocusing effect of the skull bone [4]. Nevertheless, focusing waves in complex media has been a major subject of interest in various fields of research. In optics, several techniques have been proposed and are based on wave-front shaping [5], measuring the transmission matrix of the scattering medium [6], phase conjugation [7], time-reversed ultrasonically encoded optical focusing [8], or machine learning approaches [9]. Aberration correction methods have been implemented specifically for ultrasound transcranial focusing, such as time reversal [10] or phase conjugation [11]. Nevertheless, these techniques require the use of multielement transducers and have led to an ever-increasing number of transducer elements to improve the compensation for skull aberrations: from 64 in 2000 [11] to 300 in 2003 [12] and 1372 in 2010 [13]. Using a large number of transducers imposes severe constraints on the power electronics.

Varying-thickness acoustic lenses have thus been introduced to induce phase shifts on the wave front emitted by a single-element transducer [14–16] with a limited cost and for a given frequency [17–25]. Thin lenses, based on the wrapping of the phase were first developed in the context of magnetic resonance (MR)-guided noninvasive surgery, where a flat transducer was coupled with a thin lens to allow the wave to be focused at the intended target while minimizing the size of the whole ultrasound setup and freeing space in the MR bore [26].

When it comes to achieving a multifrequency aberration correction, optics paved the way with the work conducted on chromatic aberration correction [27–29]. In medical ultrasound, such multifrequency aberration correction could be useful in the field of noninvasive neurostimulation [30], in order to find the optimal frequency to stimulate a given brain area [31,32], and for broadband transcranial therapies like brain histotripsy [33].

The aim of this work is to present the impact of phase unwrapping on acoustic lenses coupled with a geometrically focused transducer. First, numerical simulations were performed in a homogeneous medium while targeting a point laterally steered from the geometric focus of the transducer. The unwrapped and wrapped lens profiles were computed at a given frequency and the propagation of the wave through the lenses was calculated at multiple

*maxime.daniel@espci.fr
†jean-francois.aubry@espci.fr

frequencies to show the impact of phase unwrapping. Then, an application of phase unwrapping is shown for transcranial experiments performed at multiple frequencies with a single acoustic lens.

II. METHODS

A. Numerical simulations in a homogeneous medium

A proof-of-concept numerical experiment was first performed in a homogeneous medium with a 100-mm aperture and 100-mm radius of curvature spherical transducer. Its aim was to design an acoustic lens capable of focusing the wave at four different frequencies ($\nu_S = 250$, 500, 750, and 1000 kHz) on a target steered laterally from the natural focus of the transducer by 0.75 cm. All lenses were designed using the frequency $\nu_D = 500$ kHz.

Simulations were performed by solving the wave equation using pseudospectral methods. Such methods are implemented in the k-Wave MATLAB toolbox [34], which, for a lossless heterogeneous medium, solves the following set of equations [35]:

$$\frac{\partial \mathbf{u}}{\partial t} = -\frac{1}{\rho_0}\nabla\rho \quad \text{(momentum conservation)},$$

$$\frac{\partial \rho}{\partial t} = -\rho_0 \nabla\cdot\mathbf{u} - \mathbf{u}\cdot\nabla\rho_0 \quad \text{(mass conservation)},$$

$$p = c_0^2(\rho + \mathbf{d}\cdot\rho_0) \quad \text{(pressure - density relation)},$$

where $\mathbf{u}$ is the particle velocity, ρ the acoustic density, ρ_0 the equilibrium density, $\mathbf{d}$ the particle displacement, c_0 the isentropic sound speed, and p the acoustic pressure.

If the medium is homogeneous, the terms $-\mathbf{u}\cdot\nabla\rho_0$ in the mass conservation equation and $c_0^2\mathbf{d}\cdot\rho_0$ in the pressure-density relation vanish. All simulations were performed with a spatial step $\Delta x = \Delta y = \Delta z = 248$ μm, which corresponds to six points per wavelength in water at the highest frequency (1 MHz).

The algorithm developed to determine the lens profile can be described as follows:

1. A virtual source of unit amplitude (corresponding to the target) is placed in the focal plane of the transducer, but laterally steered from the geometric focus.
2. A set of virtual sensors are distributed at the surface of the transducer to record the simulated field emitted by the source at a design frequency ν_D. The phase on each sensor is computed by performing a Fourier transform on a five-period window once the steady state of the pressure signal has been reached, yielding a wrapped phase map, constrained to $[-\pi, \pi]$.
3. The phase map is transformed in a thickness map using the formula

$$e(M) = \frac{\Phi(M)}{2\pi\nu_D}\,\frac{1}{1/c_{\text{water}} - (1/c_{\text{lens}})} + K, \qquad (1)$$

where $\Phi(M)$ is the phase map, c_{water} the sound speed in water (equal to 1485 m/s), c_{lens} the sound speed in the acoustic lens material (equal to 1000 m/s), and K is a constant thickness of 2 mm added for structural stability purposes.

A second lens profile was investigated. The algorithm was the same except that the wrapped phase map was post-processed in order to obtain an unwrapped phase map, which was not constrained in the interval $[-\pi, \pi]$. Several unwrapping algorithms have been developed, based for instance on branch cuts [36] or network flow [37]. We used the unwrapping algorithm based on the transport of the intensity equation, introduced by Zhao *et al.* [38].

B. Skull imaging and acoustic modeling

Transcranial experiments were performed on three skulls (referenced as *A*, *B*, and *C*), which were provided by the Institute of Anatomy (UFR Biomédicale des Saints-Pères, Université Paris Descartes, Paris, France). Each skull was tattooed with an individual number for identification purposes, as approved by the ethics committee of the Centre du Don des Corps (Université Paris Descartes, Paris, France). Before being computed tomography (CT) scanned, each skull was degassed in water for at least 48 h at 20 mbar to remove trapped air bubbles in the skull using a vacuum pump (diaphragm pump N810.3FT.18, KNF Neuberger, Freiburg, Germany). CT scans were then acquired with a medical scanner (Revolution EVO, GE Medical Systems, Chicago, USA) at GHU Paris Psychiatrie et Neurosciences, France, with a slice thickness of 1.25 mm, an in-plane resolution of 0.625 mm, and an interslice spacing of 1.25 mm.

For acoustic parameter estimation, each CT scan was thresholded between $H_{\text{min}} = 0$ and $H_{\text{max}} = 2400$.

The conversion from Hounsfield unit (H) maps to acoustic maps was done according to the linear model described by Marsac *et al.* [39],

$$c(x,y,z) = c_{\text{water}} + (c_{\text{bone}} - c_{\text{water}})\frac{H(x,y,z) - H_{\text{min}}}{H_{\text{max}} - H_{\text{min}}},$$

$$\rho(x,y,z) = \rho_{\text{water}} + (\rho_{\text{bone}} - \rho_{\text{water}})\frac{H(x,y,z) - H_{\text{min}}}{H_{\text{max}} - H_{\text{min}}},$$

where $c_{\text{water}} = 1485$ m/s, $c_{\text{bone}} = 3100$ m/s, and $\rho_{\text{bone}} = 1900$ kg/m^3 [40].

The attenuation was neglected in this numerical model, as was done in previous work on transcranial phase estimation [41,42].

The skull acoustic maps were interpolated to an isotropic spatial resolution of six points per wavelength in water at 1 MHz, corresponding to $\Delta x = \Delta y = \Delta z = 248$ μm.

C. Transcranial acoustic lens design

The skull acoustic maps were imported in numerical simulations performed using MATLAB with the k-Wave toolbox, by solving the set of equations described in Sec. II A with a Courant-Friedrichs-Lewy number equal to 0.3 in cortical bone.

The profiles of two sets of transcranial lenses were computed using the same method as described in Sec. II A for homogeneous simulations, except that the source was placed at the geometric focus of the transducer, and the skull acoustic maps distorted the recorded phase maps. Transcranial lenses were designed with a design frequency $\nu_D = 683$ kHz, corresponding to one of the resonant frequencies of the transducer used in the experiments.

A mold was then three-dimensionally (3D) printed (Prusa i3 MK3, Prusa Research, Prague, Czech Republic) with a vertical precision of 200 μm to cast the acoustic lens. The material used to cast the lens was a silicone (Elite Double 8, Zhermack SpA, Badia Polesine, Italy) with the following acoustic properties: $c_{\text{lens}} = 1000$ m/s, $\rho_{\text{lens}} = 1040$ kg/m^3 [43]. The catalyst and the base were mixed together (1:1 ratio) and then poured into the cast.

D. Intensity map measurements and postprocessing

A custom single-element transducer with a 100-mm radius of curvature and 100-mm aperture (Imasonic, Voray-sur-l'Ognon, France) was used in the experiments. It was driven at 500, 683, and 1000 kHz, which were three of the resonance frequencies of the transducer. The input signal of the transducer was generated by an arbitrary waveform generator (33220A, Agilent Technologies, Santa Clara, CA, USA), and was then amplified (75A250, Amplifier Research, Souderton, PA, USA). The pressure field measurement was performed with a needle hydrophone (HNC-0400, Onda Corporation, Sunnyvale, CA, USA) equipped with a preamplifier (AH-2020-025, Onda Corporation, Sunnyvale, CA, USA) and an amplifier (AH-2020-DCBSW, Onda Corporation, Sunnyvale, CA, USA). The electrical signal acquired by this measurement line was digitized by a digital acquisition card (HS5, TiePie, Sneek, Netherlands). The hydrophone was mounted on a three-axis motor assembly (ESP-301, Newport, Irvine, CA, USA). Prior to the ultrasound experiments, skulls were degassed.

For each driving frequency of the transducer, four sets of experiments were performed. First, the acoustic focus location was determined by iteratively scanning around the geometric focus of the transducer, with no skull or lens interposed. The pressure signal was then recorded in a $16\lambda \times 16\lambda$ grid belonging to the focal plane and averaged 10 times with no skull. The amplitude and phase of the pressure wave were computed using the Fourier transform of the time series. The skull was then interposed between the transducer and its focal point with no lens to correct for aberrations. A 3D-printed skull holder was designed for each skull to control the position of the skull relative to the transducer. The raw pressure signal was recorded in the focal plane of the transducer and averaged 10 times. The amplitude and phase of the pressure wave were obtained by computing the Fourier transform of the time series. Finally, for each crafted lens, the wrapped and the unwrapped one, the same measurements were taken with the lens between the transducer and the skull to correct for its aberrations.

From the amplitude and phase of the pressure wave in the focal plane, the pressure amplitude was reconstructed in a 3D volume centered on the acoustic focus of the transducer using the angular spectrum method [44] and interpolated for visualization and volumetric metrics computation purposes.

E. Targeting accuracy metrics

Three different metrics were defined to quantitatively evaluate the accuracy of the aberration corrections:

(i) The maximum intensity behind the skull, obtained from 3D reconstructions

(ii) The -6 dB volume of the focal spot behind the skull obtained from 3D reconstructions, which was compared to the volume of the focal spot in water, in the absence of the skull

(iii) The normalized overlapping -6 dB volume, which corresponds to the intersection between the -6 dB volume in water with no skull and the -6 dB volume behind the skull, either with or without aberration correction. The intersection of these two volumes was normalized by the volume of the focal spot behind the skull. This metric encompasses the size and shape of the focal spot as well as its position with regards to the target, which makes it a good metric to characterize the concentration of the acoustic intensity in the vicinity of the target.

III. RESULTS

A. Numerical simulations in a homogeneous medium

Figure 1 highlights the necessity of phase unwrapping to allow a unique acoustic lens to refocus at multiple frequencies. It can be noticed that the wrapped lens presents abrupt changes in thickness, which are due to the originally computed phase being constrained in the interval $[-\pi, \pi]$. To illustrate why phase wrapped lenses do not work at all frequencies, one can consider a simplistic example consisting of a lens designed at ν_D and composed of two parts, each with a constant thickness (e_1 and e_2, respectively) such that the abrupt thickness change between the two parts corresponds to a 2π difference at ν_D. When a wave front propagates through this lens at a frequency $\nu_S \neq \nu_D$, the phase difference between the portions of the wave front

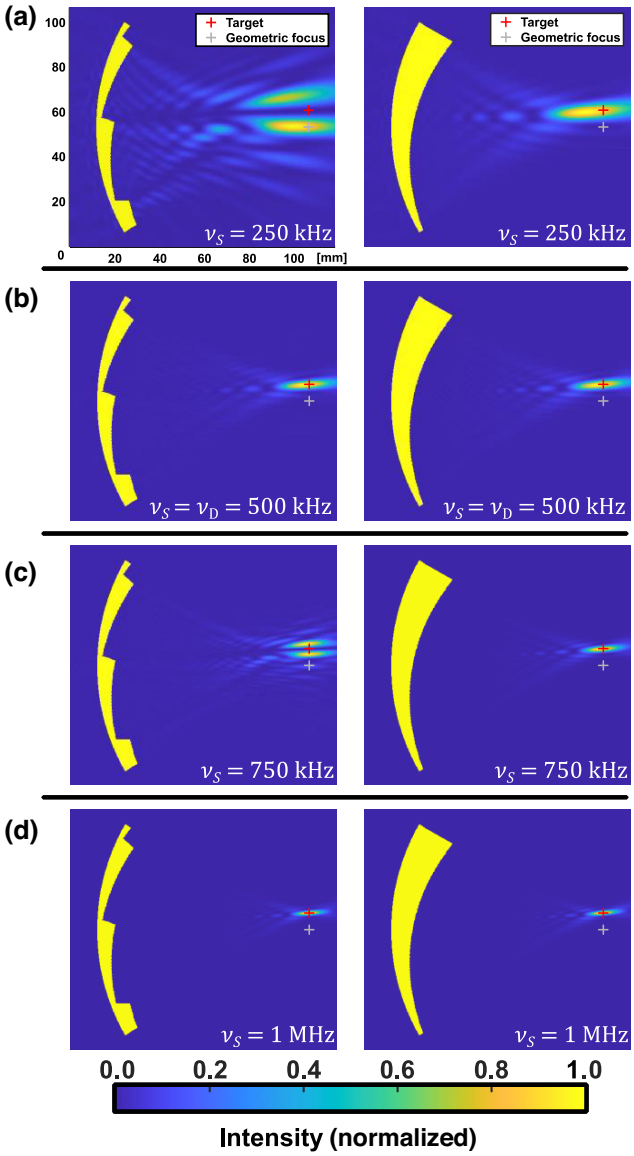

FIG. 1. Computed normalized intensity with a wrapped lens (left panel) and an unwrapped lens (right panel) designed at 500 kHz. (a) With a transducer driven at 250 kHz. (b) With a transducer driven at 500 kHz. (c) With a transducer driven at 750 kHz. (d) With a transducer driven at 1 MHz.

going through each part of the lens is, as per Eq. (1),

$$\phi_{2,v_S} - \phi_{1,v_S} = 2\pi \frac{v_S}{v_D}.$$

These thicknesses e_1 and e_2 can be considered as the lens thicknesses immediately before and after each thickness jump in the left panels of Fig. 1. If v_S is an integer multiple of v_D, as is the case in the left panels of Figs. 1(b) and 1(d), both portions of the wave front will interfere constructively. In an extreme case scenario where $v_S = 1.5\ v_D$ the wave fronts will interfere destructively and thus prevent the efficient focusing of the wave [Fig. 1(c) left panel].

On the other hand, the unwrapped lens focuses the wave effectively at any of the tested frequencies. This is because the phase unwrapping process allows the transformation of the original phase map, constrained to $[-\pi, \pi]$, to an unwrapped phase map that is not bound to this interval. As such, the unwrapped phase map $\Phi(M)$ can be linearly related to the time of flight of the signal $\Delta t(M)$, such that $\Phi(M) = 2\pi v_D \Delta t(M)$, which, when substituted into Eq. (1), allows the frequency-dependent terms to cancel out, hence yielding

$$e(M) = \frac{\Delta t(M)}{1/c_{\text{water}} - (1/c_{\text{lens}})} + K, \tag{2}$$

which is independent of the frequency, provided that the medium is nondispersive (i.e., $\Delta t(M)$ does not depend on the frequency). It was reported that the skull was weakly dispersive between 0.3 and 2 MHz [4,45], supporting the hypothesis that phase unwrapped lenses could be able to correct for skull aberrations within the same range of frequency.

B. Transcranial experimental validation at the design frequency of the lens

The intensity maps measured at the design frequency of the lenses are shown on Fig. 2 for skull *A*. The results for the other skulls are available in the Supplemental Material [46].

Uncorrected scans [Fig. 2(a)] exhibit a degraded focusing due to the presence of the skull. Two main spots are visible on Fig. 2(a) in the focal plane of the transducer.

Wrapped [Fig. 2(c)] and unwrapped lenses [Fig. 2(b)] allow the correction for skull aberrations at the design frequency of the lens. Higher secondary lobes can be seen on the measurement made with the wrapped lens. The irregularities induced by the phase jumps are not supposed to disrupt the coherence of the wave as they correspond to a 2π phase difference. Nevertheless, it can be hypothesized that the irregularities induce refraction. Such refraction was not taken into account in the design of the lens. Iterative simulation-based optimization could help mitigate this effect. This is beyond the current work and would require an extension of the work previously introduced in homogenous media [47] and would benefit from the reduction of the simulation time required for transcranial simulations [48].

C. Multifrequency transcranial focusing experiments

The intensity maps at 500 kHz obtained with lenses designed at 683 kHz are shown in Fig. 3. The results for the other skulls at 500 kHz are available in the Supplemental Material [46].

The uncorrected intensity map at 500 kHz [Fig. 3(a)] is less distorted than the one obtained at 683 kHz [Fig. 2(a)]

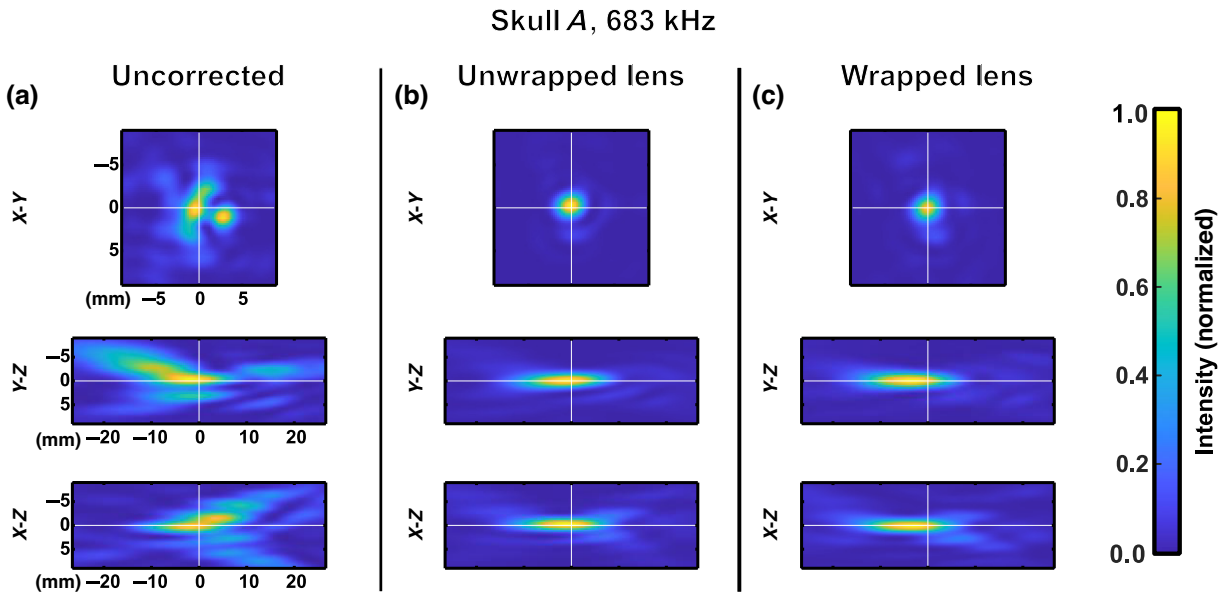

FIG. 2. Measured intensity at 683 kHz for each condition on skull *A*. The white crosses are centered on the location of the acoustic focus in water. (a) Measured intensity with no lens. (b) Measured intensity with a phase unwrapped lens. (c) Measured intensity with a phase wrapped lens.

and looks better than that of the wrapped lens [Fig. 3(c)], the latter being strongly affected by the frequency change, as explained in Sec. III A. The unwrapped lens, however, still allows the correction for the skull aberrations at this frequency [Fig. 3(b)].

The intensity maps obtained at 1 MHz with the same lenses are shown in Fig. 4. The results for the other skulls at 1 MHz are available in the Supplemental Material [46].

The uncorrected intensity map [Fig. 4(a)] is highly distorted by the presence of the skull at 1 MHz, highlighting the need for aberration correction at high frequency. The wrapped lens designed at 683 kHz [Fig. 4(c)] is not capable of correcting for such aberrations at 1 MHz for the same reason as previously mentioned. The unwrapped lens [Fig. 4(b)] still exhibits a tight focusing at this frequency, thus achieving broadband aberration correction.

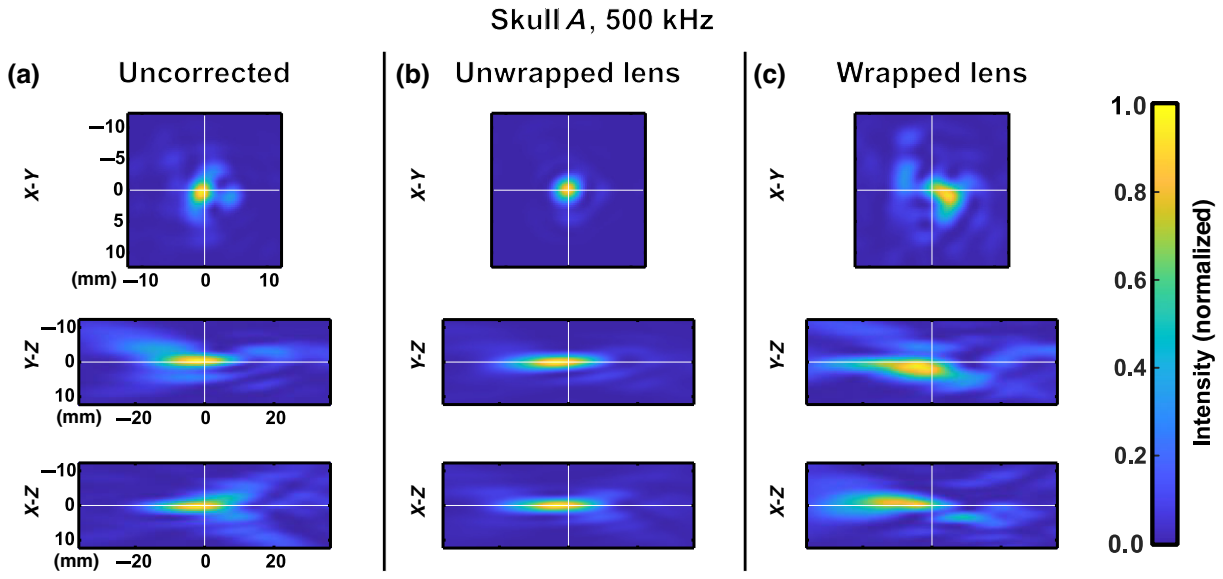

FIG. 3. Measured intensity at 500 kHz for each condition on skull *A*. The white crosses are centered on the location of the acoustic focus in water. (a) Measured intensity with no lens. (b) Measured intensity with a phase unwrapped lens. (c) Measured intensity with a phase wrapped lens.

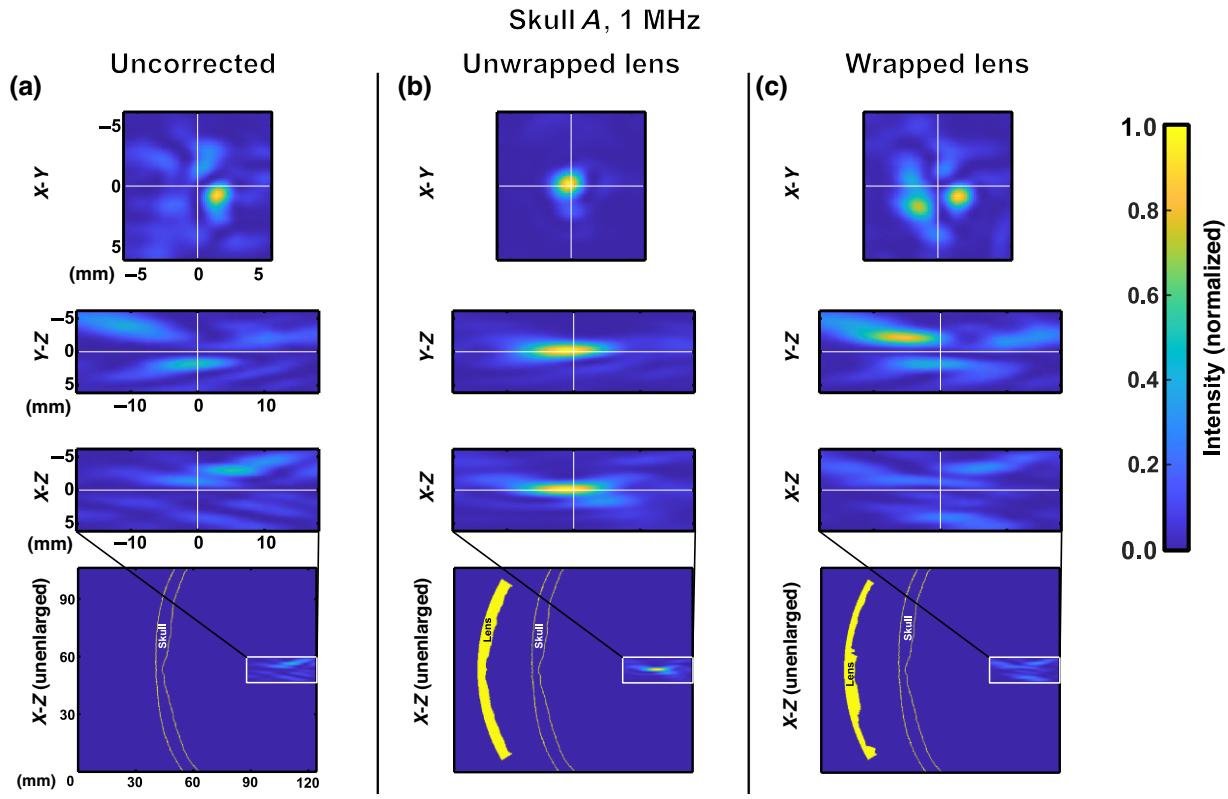

FIG. 4. Measured intensity at 1 MHz for each condition on skull *A*. The white crosses are centered on the location of the acoustic focus in water. (a) Measured intensity with no lens. (b) Measured intensity with a phase unwrapped lens. (c) Measured intensity with a phase wrapped lens. For each condition, a large field of view version of the intensity map in the X-Z plane is provided to visualize the skull and lens geometry.

The broadband correction highlighted by Figs. 3 and 4 for the unwrapped lens suggests that dispersion is negligible in skull and silicone for this frequency range.

The inability of wrapped lenses to compensate for skull aberrations at frequencies different than their design frequency can also be explained in the light of the Rayleigh criterion, which states that an optical instrument would offer performance close to that of an ideal system as long as the optical path difference remains below one quarter of a wavelength [49]. In our case the phase difference induced by the lens should remain below $\pi/2$. As discussed previously, a 2π phase jump obtained at ν_D induces a phase shift of $2\pi(\nu_S/\nu_D)$ when a wave propagates through the lens at ν_S. The phase difference can be expressed as

$$\Delta\phi_{\nu_D,\nu_S} = 2\pi \left| \frac{\nu_S}{\nu_D} - 1 \right|.$$

Using a design frequency of $\nu_D = 683$ kHz, this corresponds to $\Delta\phi_{\nu_D,\nu_S} = 1.68$ rad and $\Delta\phi_{\nu_D,\nu_S} = 2.92$ rad at $\nu_S = 500$ kHz and $\nu_S = 1$ MHz, respectively. Neither of these values fit the Rayleigh criterion, which might explain the significant defocusing of the wave when the design frequency of the wrapped lens differs from the driving frequency of the transducer.

D. Targeting accuracy metrics

Figure 5 represents the means and standard deviations of the metrics on three different skulls, for the three frequencies. The detailed results for each skull are available in Table SI in the Supplemental Material [46]. The -6 dB volume [Fig. 5(a)] shows that both the wrapped lenses and unwrapped lenses work at the design frequency of the lens, since the sizes of the focal spots behind the skull are similar to the size of the reference focal spot. This is true for each of the three skulls tested, as assessed by the low standard deviations for both lenses. As could be already seen qualitatively from the intensity maps in Secs. III B and III C, Fig. 5(a) confirms that the unwrapped lenses are able to restore a tight focusing at each of the three frequencies.

The intensity maps displayed in Sec. III C might suggest that correcting for skull aberrations is not always necessary at low frequencies. Nonetheless, Fig. 5(a) disproves this hypothesis by highlighting a higher standard deviation across the uncorrected cases. At 500 kHz, the standard deviation corresponds to 105% and 7% of the reference value without correction and with the unwrapped lens, respectively (see Table SI in the Supplemental Material [46]).

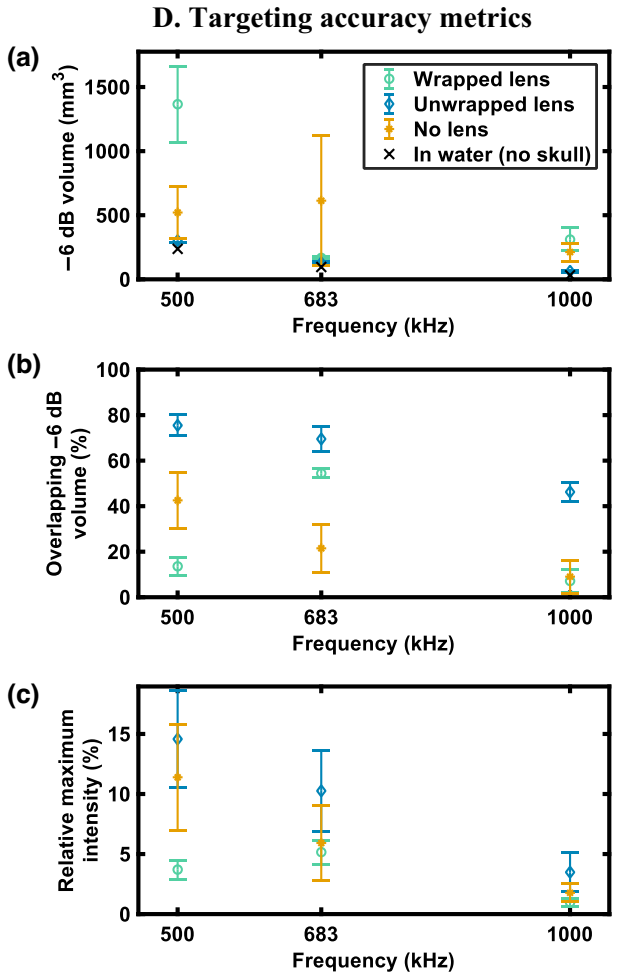

FIG. 5. Mean and standard deviation of the metrics obtained from the measurements made on three skulls. (a) −6 dB volume in cubic millimeters computed from the 3D field reconstructions. (b) Normalized overlapping −6 dB volume computed from the 3D field reconstructions. (c) Maximum intensity in the reconstructed volume normalized by the maximum intensity in water. For (b),(c) the result in water with no skull is not shown since it is equal to 100% by definition of the metrics.

The overlapping −6 dB volume plot [Fig. 5(b)] and the maximum intensity measured behind the skull [Fig. 5(c)] confirm the broadband aspect of the aberration correction of the unwrapped acoustic lens.

The maximum intensity for the wrapped lens is lower, even at its design frequency [Fig. 5(c)], with an average 49% relative drop compared to the unwrapped lens (see Table SI in the Supplemental Material [46]). This demonstrates that even when focusing the wave at a single frequency, unwrapping the phase can significantly improve the intensity at the focus. We attribute this phenomenon to refraction at the thickness jump in the wrapped lenses.

The significant standard deviations of the maximum intensity retrieved behind the skulls shown in Fig. 5(c), even when correcting for aberrations with phase unwrapped lenses, are hypothesized to be because each skull is intrinsically more or less attenuating due to its thickness and internal geometry. In addition, a decrease of the maximum retrieved intensity as the frequency increases is in line with the increase of the attenuation of the skull bone with the frequency [4,50].

IV. DISCUSSION AND CONCLUSIONS

This work demonstrates the advantage of phase unwrapping for the design of multifrequency acoustic lenses.

Phase unwrapping is shown to both improve the performance of single-frequency lenses and enable multifrequency lenses in homogenous lateral beam steering simulations and in transcranial focusing experiments. This is because the phase received on the surface of a transducer is not always contained in a 2π interval after propagation of the wave from its initial target.

The presence of thickness jumps on the surface of the lens depends on many parameters, among which is the geometry of the transducer. If the transducer is not spherical, as is the case in many transcranial lens studies [15,51,52], the phase shifts to focus the wave will inevitably span an interval larger than 2π. In the case of a spherical transducer, the aperture plays a role in the presence of phase jumps, since a larger transducer aperture will include a larger section of the skull and a larger span of the phase required to refocus the wave [33,39,41,53–57]. The geometry of the section of the skull through which the wave propagates will also play a role, since a skull section of quasiuniform thickness will require little correction compared with a more undulating skull [58]. For simple cases, e.g., considering a small-aperture spherical transducer focusing through a slightly aberrating medium at a low frequency, the phase maps might be entirely contained in a 2π interval. In such cases, limiting the number of residual phase jumps may be done by simply adjusting the phase reference.

According to Eq. (2), unwrapped phase masks can be obtained from times of flight. As such, it could be possible to use ray-tracing simulations to obtain the phase masks in a more computationally efficient way [41,59].

A limitation of phase unwrapped lenses is that, provided that the unwrapped phase span is an interval larger than 2π, the resulting lens will be thicker than the one that could be obtained by wrapping the phase, according to Eq. (1).

Owing to their broadband properties, unwrapped acoustic lenses could be used to adjust the frequency with a fixed setup for transcranial biomedical applications such as deep brain ultrasound stimulation [32,60–63] or high-intensity focused ultrasound therapies [64,65]. Broadband acoustic lenses could also help increase the data transfer rate of spatially selective airborne ultrasound transmission with a limited number of sources [66–68].

Since the skull bone has a high impedance compared with that of water, it could be possible to couple such acoustic lenses with metamaterials aimed at enhancing the transmission efficacy of ultrasound through biological layers [69].

ACKNOWLEDGMENTS

The authors thank Thomas Manuel for proofreading this article. This work was supported by the "Agence Nationale de la Recherche" under the program "Ultrastim" [Program No. ANR-20-CE19-0013].

[1] Y. Kim, Advances in MR image-guided high-intensity focused ultrasound therapy, Int. J. Hyperthermia **31**, 225 (2015).
[2] E. S. Ebbini and G. Ter Haar, Ultrasound-guided therapeutic focused ultrasound: Current status and future directions, Int. J. Hyperthermia **31**, 77 (2015).
[3] D. Tyshlek, J.-F. Aubry, G. ter Haar, A. Hananel, J. Foley, M. Eames, N. Kassell, and H. H. Simonin, Focused ultrasound development and clinical adoption: 2013 update on the growth of the field, J. Ther. Ultrasound **2**, 2 (2014).
[4] F. J. Fry and J. E. Barger, Acoustical properties of the human skull, J. Acoust. Soc. Am. **63**, 1576 (1978).
[5] A. Sanjeev, V. Trivedi, and Z. Zalevsky, Optical reciprocity induced wavefront shaping for axial and lateral shifting of focus through a scattering medium, Sci. Rep. **12**, 6387 (2022).
[6] S. M. Popoff, G. Lerosey, R. Carminati, M. Fink, A. C. Boccara, and S. Gigan, Measuring the transmission matrix in optics: An approach to the study and control of light propagation in disordered media, Phys. Rev. Lett. **104**, 100601 (2010).
[7] Z. Yaqoob, D. Psaltis, M. S. Feld, and C. Yang, Optical phase conjugation for turbidity suppression in biological samples, Nat. Photonics **2**, 110 (2008).
[8] X. Xu, H. Liu, and L. V. Wang, Time-reversed ultrasonically encoded optical focusing into scattering media, Nat. Photonics **5**, 154 (2011).
[9] M. Lyu, H. Wang, G. Li, S. Zheng, and G. Situ, Learning-based lensless imaging through optically thick scattering media, Adv. Photonics **1**, 036002 (2019).
[10] J.-F. Aubry, M. Tanter, M. Pernot, J.-L. Thomas, and M. Fink, Experimental demonstration of noninvasive transskull adaptive focusing based on prior computed tomography scans, J. Acoust. Soc. Am. **113**, 84 (2003).
[11] G. T. Clement, J. Sun, T. Giesecke, and K. Hynynen, A hemisphere array for non-invasive ultrasound brain therapy and surgery, Phys. Med. Biol. **45**, 3707 (2000).
[12] M. Pernot, J.-F. Aubry, M. Tanter, J.-L. Thomas, and M. Fink, High power transcranial beam steering for ultrasonic brain therapy, Phys. Med. Biol. **48**, 2577 (2003).
[13] J. Song and K. Hynynen, Feasibility of using lateral mode coupling method for a large scale ultrasound phased array for noninvasive transcranial therapy, IEEE Trans. Biomed. Eng. **57**, 124 (2010).
[14] R. Lalonde and J. W. Hunt, Variable frequency field conjugate lenses for ultrasound hyperthermia, IEEE Trans. Ultrason., Ferroelectr., Freq. Control **42**, 825 (1995).
[15] Z. Hu, Y. Yang, L. Xu, Y. Hao, and H. Chen, Binary acoustic metasurfaces for dynamic focusing of transcranial ultrasound, Front. Neurosci. **16**, 984953 (2022).
[16] M. D. Brown, B. T. Cox, and B. E. Treeby, Design of multi-frequency acoustic kinoforms, Appl. Phys. Lett. **111**, 244101 (2017).
[17] R. E. Beard, R. L. Magin, L. A. Frizzell, and C. A. Cain, An annular focus ultrasonic lens for local hyperthermia treatment of small tumors, Ultrasound Med. Biol. **8**, 177 (1982).
[18] R. J. Lalonde, A. Worthington, and J. W. Hunt, Field conjugate acoustic lenses for ultrasound hyperthermia, IEEE Trans. Ultrason., Ferroelectr., Freq. Control **40**, 592 (1993).
[19] X. Wu and M. Sherar, Theoretical evaluation of moderately focused spherical transducers and multi-focus acoustic lens/transducer systems for ultrasound thermal therapy, Phys. Med. Biol. **47**, 1603 (2002).
[20] G. Maimbourg, A. Houdouin, T. Deffieux, M. Tanter, and J.-F. Aubry, Steering capabilities of an acoustic lens for transcranial therapy: Numerical and experimental studies, IEEE Trans. Biomed. Eng. **67**, 27 (2020).
[21] S. Jiménez-Gambín, N. Jiménez, J. M. Benlloch, and F. Camarena, Holograms to focus arbitrary ultrasonic fields through the skull, Phys. Rev. Appl. **12**, 014016 (2019).
[22] S. Jiménez-Gambín, N. Jiménez, and F. Camarena, Transcranial focusing of ultrasonic vortices by acoustic holograms, Phys. Rev. Appl. **14**, 054070 (2020).
[23] M. D. Brown, Phase and amplitude modulation with acoustic holograms, Appl. Phys. Lett. **115**, 053701 (2019).
[24] M. D. Brown, B. T. Cox, and B. E. Treeby, Stackable acoustic holograms, Appl. Phys. Lett. **116**, 261901 (2020).
[25] K. Melde, A. G. Mark, T. Qiu, and P. Fischer, Holograms for acoustics, Nature **537**, 518 (2016).
[26] T. Fjield, C. E. Silcox, and K. Hynynen, Low-profile lenses for ultrasound surgery, Phys. Med. Biol. **44**, 1803 (1999).
[27] H. Zhou, L. Chen, F. Shen, K. Guo, and Z. Guo, Broadband achromatic metalens in the midinfrared range, Phys. Rev. Appl. **11**, 024066 (2019).
[28] P. Wang, N. Mohammad, and R. Menon, Chromatic-aberration-corrected diffractive lenses for ultra-broadband focusing, Sci. Rep. **6**, 1 (2016).
[29] E. J. Fernández, A. Unterhuber, B. Považay, B. Hermann, P. Artal, and W. Drexler, Chromatic aberration correction of the human eye for retinal imaging in the near infrared, Opt. Express **14**, 6213 (2006).
[30] C. Constans, T. Deffieux, P. Pouget, M. Tanter, and J.-F. Aubry, A 200–1380-kHz quadrifrequency focused ultrasound transducer for neurostimulation in rodents and primates: Transcranial in vitro calibration and numerical study of the influence of skull cavity, IEEE Trans. Ultrason., Ferroelectr., Freq. Control **64**, 717 (2017).
[31] M. Plaksin, S. Shoham, and E. Kimmel, Intramembrane cavitation as a predictive bio-piezoelectric mechanism for ultrasonic brain stimulation, Phys. Rev. X **4**, 011004 (2014).

[32] R. L. King, J. R. Brown, W. T. Newsome, and K. B. Pauly, Effective parameters for ultrasound-induced in vivo neurostimulation, Ultrasound Med. Biol. **39**, 312 (2013).

[33] N. Lu, T. L. Hall, J. R. Sukovich, S. W. Choi, J. Snell, N. McDannold, and Z. Xu, Two-step aberration correction: Application to transcranial histotripsy, Phys. Med. Biol. **67**, 125009 (2022).

[34] B. E. Treeby and B. T. Cox, k-Wave: MATLAB toolbox for the simulation and reconstruction of photoacoustic wave fields, J. Biomed. Opt. **15**, 021314 (2010).

[35] B. E. Treeby, J. Jaros, A. P. Rendell, and B. T. Cox, Modeling nonlinear ultrasound propagation in heterogeneous media with power law absorption using a k-space pseudospectral method, J. Acoust. Soc. Am. **131**, 4324 (2012).

[36] D. Zheng and F. Da, A novel algorithm for branch cut phase unwrapping, Opt. Lasers Eng. **49**, 609 (2011).

[37] M. Costantini, A novel phase unwrapping method based on network programming, IEEE Trans. Geosci. Remote Sens. **36**, 813 (1998).

[38] Z. Zhao, H. Zhang, Z. Xiao, H. Du, Y. Zhuang, C. Fan, and H. Zhao, Robust 2D phase unwrapping algorithm based on the transport of intensity equation, Meas. Sci. Technol. **30**, 015201 (2019).

[39] L. Marsac, D. Chauvet, R. La Greca, A.-L. Boch, K. Chaumoitre, M. Tanter, and J.-F. Aubry, Ex vivo optimisation of a heterogeneous speed of sound model of the human skull for non-invasive transcranial focused ultrasound at 1 MHz, Int. J. Hyperthermia **33**, 635 (2017).

[40] F. A. Duck, *Physical Properties of Tissue: A Comprehensive Reference Book* (Academic Press, London, 1990).

[41] T. Bancel, A. Houdouin, P. Annic, I. Rachmilevitch, Y. Shapira, M. Tanter, and J.-F. Aubry, Comparison between ray-tracing and full-wave simulation for transcranial ultrasound focusing on a clinical system using the transfer matrix formalism, IEEE Trans. Ultrason., Ferroelectr., Freq. Control **68**, 2554 (2021).

[42] N. McDannold, P. J. White, and R. Cosgrove, Elementwise approach for simulating transcranial MRI-guided focused ultrasound thermal ablation, Phys. Rev. Res. **1**, 033205 (2019).

[43] G. Maimbourg, A. Houdouin, T. Deffieux, M. Tanter, and J.-F. Aubry, 3D-printed adaptive acoustic lens as a disruptive technology for transcranial ultrasound therapy using single-element transducers, Phys. Med. Biol. **63**, 025026 (2018).

[44] X. Zeng and R. J. McGough, Evaluation of the angular spectrum approach for simulations of near-field pressures, J. Acoust. Soc. Am. **123**, 68 (2008).

[45] S. Pichardo, V. W. Sin, and K. Hynynen, Multi-frequency characterization of the speed of sound and attenuation coefficient for longitudinal transmission of freshly excised human skulls, Phys. Med. Biol. **56**, 219 (2010).

[46] See Supplemental Material at http://link.aps.org/supplemental/10.1103/PhysRevApplied.21.014011 for intensity maps obtained on two other skulls at the three tested frequencies; quantitative results for each tested skull.

[47] M. D. Brown, B. T. Cox, and B. E. Treeby, Binary volume acoustic holograms, Phys. Rev. Appl. **19**, 044032 (2023).

[48] G. Maimbourg, J. Guilbert, T. Bancel, A. Houdouin, G. Raybaud, M. Tanter, and J.-F. Aubry, Computationally efficient transcranial ultrasonic focusing: Taking advantage of the high correlation length of the human skull, IEEE Trans. Ultrason., Ferroelectr., Freq. Control **67**, 1993 (2020).

[49] A. E. Conrady and R. Kingslake, *Applied Optics and Optical Design* (Dover publications, New-York, 1992).

[50] H. Estrada, J. Rebling, J. Turner, and D. Razansky, Broadband acoustic properties of a murine skull, Phys. Med. Biol. **61**, 1932 (2016).

[51] G. Kook, Y. Jo, C. Oh, X. Liang, J. Kim, S.-M. Lee, S. Kim, J.-W. Choi, and H. J. Lee, Multifocal skull-compensated transcranial focused ultrasound system for neuromodulation applications based on acoustic holography, Microsyst. Nanoeng. **9**, 1 (2023).

[52] D. Andrés, N. Jiménez, J. M. Benlloch, and F. Camarena, Numerical study of acoustic holograms for deep-brain targeting through the temporal bone window, Ultrasound Med. Biol. **48**, 872 (2022).

[53] M. Wintermark, N. J. Tustison, W. J. Elias, J. T. Patrie, W. Xin, N. Demartini, M. Eames, S. Sumer, B. Lau, A. Cupino, *et al.*, T1-weighted MRI as a substitute to CT for refocusing planning in MR-guided focused ultrasound, Phys. Med. Biol. **59**, 3599 (2014).

[54] G. W. Miller, M. Eames, J. Snell, and J.-F. Aubry, Ultrashort echo-time MRI versus CT for skull aberration correction in MR-guided transcranial focused ultrasound: In vitro comparison on human calvaria: UTE-based skull aberration correction for MR-guided HIFU, Med. Phys. **42**, 2223 (2015).

[55] G. F. Pinton, J.-F. Aubry, and M. Tanter, Direct phase projection and transcranial focusing of ultrasound for brain therapy, IEEE Trans. Ultrason., Ferroelectr., Freq. Control **59**, 1149 (2012).

[56] F. Marquet, M. Pernot, J.-F. Aubry, G. Montaldo, L. Marsac, M. Tanter, and M. Fink, Non-invasive transcranial ultrasound therapy based on a 3D CT scan: Protocol validation and in vitro results, Phys. Med. Biol. **54**, 2597 (2009).

[57] E. A. Kaye, Y. Hertzberg, M. Marx, B. Werner, G. Navon, M. Levoy, and K. B. Pauly, Application of Zernike polynomials towards accelerated adaptive focusing of transcranial high intensity focused ultrasound, Med. Phys. **39**, 6254 (2012).

[58] D. Attali, T. Tiennot, M. Schafer, E. Fouragnan, J. Sallet, C. F. Caskey, R. Chen, G. Darmani, E. J. Bubrick, C. Butler, *et al.*, Three-layer model with absorption for conservative estimation of the maximum acoustic transmission coefficient through the human skull for transcranial ultrasound stimulation, Brain Stimul. **16**, 48 (2023).

[59] T. Wang and Y. Jing, Transcranial ultrasound imaging with speed of sound-based phase correction: A numerical study, Phys. Med. Biol. **58**, 6663 (2013).

[60] Y. Tufail, A. Matyushov, N. Baldwin, M. L. Tauchmann, J. Georges, A. Yoshihiro, S. I. H. Tillery, and W. J. Tyler, Transcranial pulsed ultrasound stimulates intact brain circuits, Neuron **66**, 681 (2010).

[61] S.-S. Yoo, A. Bystritsky, J.-H. Lee, Y. Zhang, K. Fischer, B.-K. Min, N. J. McDannold, A. Pascual-Leone, and F. A.

Jolesz, Focused ultrasound modulates region-specific brain activity, NeuroImage **56**, 1267 (2011).

[62] T. Deffieux, Y. Younan, N. Wattiez, M. Tanter, P. Pouget, and J.-F. Aubry, Low-intensity focused ultrasound modulates monkey visuomotor behavior, Curr. Biol. **23**, 2430 (2013).

[63] P.-F. Yang, M. A. Phipps, A. T. Newton, S. Jonathan, T. J. Manuel, J. C. Gore, W. A. Grissom, C. F. Caskey, and L. M. Chen, Differential dose responses of transcranial focused ultrasound at brain regions indicate causal interactions, Brain Stimul. **15**, 1552 (2022).

[64] W. J. Elias, N. Lipsman, W. G. Ondo, P. Ghanouni, Y. G. Kim, W. Lee, M. Schwartz, K. Hynynen, A. M. Lozano, B. B. Shah, *et al.*, A randomized trial of focused ultrasound thalamotomy for essential tremor, N. Engl. J. Med. **375**, 730 (2016).

[65] R. Martínez-Fernández, J. U. Máñez-Miró, R. Rodríguez-Rojas, M. del Álamo, B. B. Shah, F. Hernández-Fernández, J. A. Pineda-Pardo, M. H. G. Monje, B. Fernández-Rodríguez, S. A. Sperling, *et al.*, Randomized trial of focused ultrasound subthalamotomy for Parkinson's disease, N. Engl. J. Med. **383**, 2501 (2020).

[66] A. Derode, A. Tourin, J. de Rosny, M. Tanter, S. Yon, and M. Fink, Taking advantage of multiple scattering to communicate with time-reversal antennas, Phys. Rev. Lett. **90**, 014301 (2003).

[67] W. Jiang and W. M. D. Wright, Multichannel ultrasonic data communications in air using range-dependent modulation schemes, IEEE Trans. Ultrason., Ferroelectr., Freq. Control **63**, 147 (2016).

[68] S. Holm, O. B. Hovind, S. Rostad, and R. Holm, in *Proceedings. (ICASSP '05). IEEE International Conference on Acoustics, Speech, and Signal Processing, 2005* (IEEE, Philadelphia, Pennsylvania, USA, 2005), Vol. 3, pp. 957–960.

[69] J. Wang, F. Allein, N. Boechler, J. Friend, and O. Vazquez-Mena, Design and fabrication of negative-refractive-index metamaterial unit cells for near-megahertz enhanced acoustic transmission in biomedical ultrasound applications, Phys. Rev. Appl. **15**, 024025 (2021).